catalysts

MDPI

Article

Performance and Mechanism of Monolithic Co-Doped Nickel–Iron Foam Catalyst for Highly Efficient Activation of PMS in Degrading Chlortetracycline in Water

Yiqiong Yang, Xuyang Gao, Juan Han, Mingkun Cao, Li Qing, Liren Yu and Xiaodong Zhang *

School of Environment and Architecture, University of Shanghai for Science and Technology, Shanghai 200093, China

* Correspondence: fatzhxd@126.com; Tel.: +86-159-2126-7160

Abstract

Metal–organic framework (MOF) materials were extensively studied in the removal of pollutants in wastewater. However, catalysts in the powder form usually suffered from the strong tendency to agglomerate and the intricate operation for recycling, which significantly limited their practical application. In comparison, monolithic catalysts with their high macroscopic operability and recoverability as well as impressive specific surface area have attracted tremendous attention in recent years. To address these issues, a monolithic Fe-based catalyst was prepared via in situ synthesis, using nickel–iron foam (NFF) as the substrate with cobalt (Co) incorporation. XPS analysis showed that Co doping enhanced the synergistic interaction among Fe, Ni, and Co, accelerating the redox cycle among species, thus improving electron transfer and laying a kinetic foundation for efficient peroxymonosulfate (PMS) activation. Quenching experiments and EPR indicated singlet oxygen ($^1O_2$) as the main reactive species; Co doping shifted the degradation pathway from radicals to non-radicals. Under optimized conditions (PMS: 0.08 mmol/L; catalyst: 1 cm^2; initial Chlortetracycline (CTC): 50 mg/L), 95.7% CTC degradation was achieved within 60 min, and efficiency only dropped to 90.5% after 5 cycles. This catalyst provided theoretical and technical support for the application of monolithic MOF-derived catalysts and highly efficient PMS activators.

Keywords: monolithic iron-based catalyst; peroxymonosulfate activation; chlortetracycline degradation; non-radical pathway

Check for updates

Academic Editor: Stanisław Wacławek

Received: 4 November 2025
Revised: 3 December 2025
Accepted: 5 December 2025
Published: 1 January 2026

Copyright: © 2026 by the authors. Licensee MDPI, Basel, Switzerland. This article is an open access article distributed under the terms and conditions of the Creative Commons Attribution (CC BY) license.

1. Introduction

Tetracycline antibiotics are the second most widely used antibiotics globally due to their high antimicrobial activity against various bacterial infections [1]. Among them, Chlortetracycline (CTC) exhibits inhibitory effects on both Gram-positive and Gram-negative bacteria. It is widely used in swine feed as a growth promoter and for the treatment of diseases such as avian typhoid and bacillary dysentery in livestock and poultry. According to the literature, residual CTC concentrations in environmental water are lower than 0.5 μg/L. China's Comprehensive Sewage Discharge Standard (GB 21903-2008) [2] of Water Pollutants for Pharmaceutical Industry should be implemented. Therefore, given the health risks associated with the introduction of antibiotics into the environment, the removal of CTC from water has emerged as a key research focus in the fields of environmental engineering and environmental chemistry in recent years.

Sulfate radical-based advanced oxidation process (SR-AOP) is an oxidation treatment method that has attracted much attention in recent years. It has wide pH adaptability, longer radical half-life, and higher redox potential (2.5–3.1 V), and is considered an effective way to treat refractory pollutants in water. Due to the high chemical stability of peroxymonosulfate (PMS) and its weak oxidation capacity for organic pollutants in water, it is necessary to activate PMS to generate $SO_4^{\bullet-}$ through activation reactions to degrade organic pollutants. Studies have shown that transition metal activation technologies (using metals such as Co, Ni, Fe, and Cu) can effectively activate PMS to produce highly oxidizing radicals, such as sulfate radical ($SO_4^{\bullet-}$) and hydroxyl radical (•OH) [3]. Among various transition metal ions, Co^{2+} as homogeneous catalysts exhibit the highest catalytic activity for PMS activation. Therefore, activating PMS with cobalt-based catalysts is a promising strategy, and finding more efficient and stable cobalt-based materials has become a key research focus [4].

Metal–organic frameworks (MOFs) are a new type of nanoporous inorganic–organic hybrid materials, with representative members such as MIL series (e.g., MIL-101, MIL-88), UiO-66, and ZIF-67 widely investigated in aqueous oxidation processes due to their structural versatility and functional tunability [5,6]. Among them, MIL-101 (Fe) is composed of iron ions and carboxylic acid ligands, possessing a high specific surface area, a tunable pore structure, and excellent stability as well as regenerability—advantages shared by many MOFs like UiO-66 (renowned for its exceptional chemical and thermal stability) and MIL-88 (favored for its flexible framework and adjustable pore sizes) [7–10]. When equipped with highly dispersed Co sites, MIL-101 allows for the uniform dispersion of Co ions, a feature also observed in Co-based MOFs such as ZIF-67 (a zeolitic imidazolate framework with intrinsic Co centers) [11], thus making it a suitable support for cobalt-based catalysts. However, similar to most nano powder MOFs (including MIL-88, UiO-66, and ZIF-67), powder materials have relatively large limitations in practice [12,13]. MOFs with nano powder microcrystalline structure are easy to agglomerate, which will cause secondary pollution, pipeline blockage, and reduce processing efficiency—a common challenge that has restricted the practical application of many powdered MOF-based catalysts. An et al. [14] successfully prepared a monolithic iron-based catalyst using oxidized waste iron scraps as the substrate, and it showed excellent catalytic activity in the catalytic ozonation of industrial wastewater after biochemical treatment, providing a viable strategy to address the agglomeration issue of powder MOFs. The synergistic effect enhances the activity, stability, and reaction rate of catalysts through the interactions between two or more distinct components [15]. In addition, Zhang et al. [16] synthesized a modified MIL-101 with simultaneous carbonization and nitrogen doping, which indicated that nitrogen doping can significantly improve the electron transfer efficiency of MOF materials. Therefore, inspired by these studies and the structural merits of various MOFs in aqueous oxidation, we expect that monolithic MOF catalysts with excellent performance can be prepared by N modification and introducing Co source on MOF materials to improve PMS activation efficiency.

In this study, N-101-NFF (a monolithic material) was synthesized as the precursor using nickel–iron foam (NFF) as the substrate by an in situ synthesis. To explore the synergistic effect between different metals, a Co source was introduced on the basis of N-101-NFF, and N-101-NFF (Co_x) with excellent catalytic performance was successfully prepared. Subsequently, N-101-NFF (Co_x) was characterized by XRD, FT-IR, SEM, TEM, etc., to investigate the effects of different Co doping ratios on the material's performance and structure. The factors that may affect its catalytic efficiency were discussed, including experimental parameters, inorganic anions, organic matter, pH value, water body, etc. LC-MS was used to analyze the intermediates and deduce the CTC degradation pathway, and analyze the toxicity of the intermediates. Moreover, the CTC degradation performance in a simulated continuous-flow practical scenario was evaluated using a fixed-bed device.

2. Results and Discussion

2.1. Characterization

2.1.1. XRD and FT-IR

The phase structure of the samples was characterized by XRD. As shown in Figure 1a, the characteristic peaks of the sample appearing at 44.3°, 51.7°, and 76.2° could be assigned to the (111), (200), and (220) lattice planes, corresponding to the reflections of the face-centered cubic (fcc) nickel phase (JCPDS Card No. 87-0712), respectively [17]. Based on the ionic radii, Fe (Fe^{2+}: 0.078 nm, Fe^{3+}: 0.064 nm) has a smaller ionic radius compared to Ni (Ni^{2+}: 0.069 nm), leading to a contraction of the lattice and a decrease in the 2θ value. In contrast, Co (Co^{2+}: 0.074 nm) has a slightly larger ionic radius than Ni, leading to an increase in the 2θ value upon doping [18,19]. As presented in Figure 1a, with the introduction of Fe ions, a shift in diffraction peak was detected, indicating that Fe was incorporated into the cubic crystal structure of nickel via a substitution mechanism [20]. In addition, as the Co doping content increased, a shift in the material's diffraction peaks toward higher 2θ angles was also observed, implying that Co atoms were stably present in the NFF lattice in a doped state [21]. Owing to the similar ionic radii of Co^{2+}, Ni^{2+}, and Fe^{2+}, the incorporation of Co did not alter the original crystal phase of NFF [22–24]. When the molar ratio of Co:Fe exceeded 0.05:1, the diffraction peak intensity of N-101-NFF ($Co_{0.1}$) and N-101-NFF ($Co_{0.2}$) showed a gradual decrease, which indicated that excessive Co doping exerted an adverse effect on the crystallinity of the material.

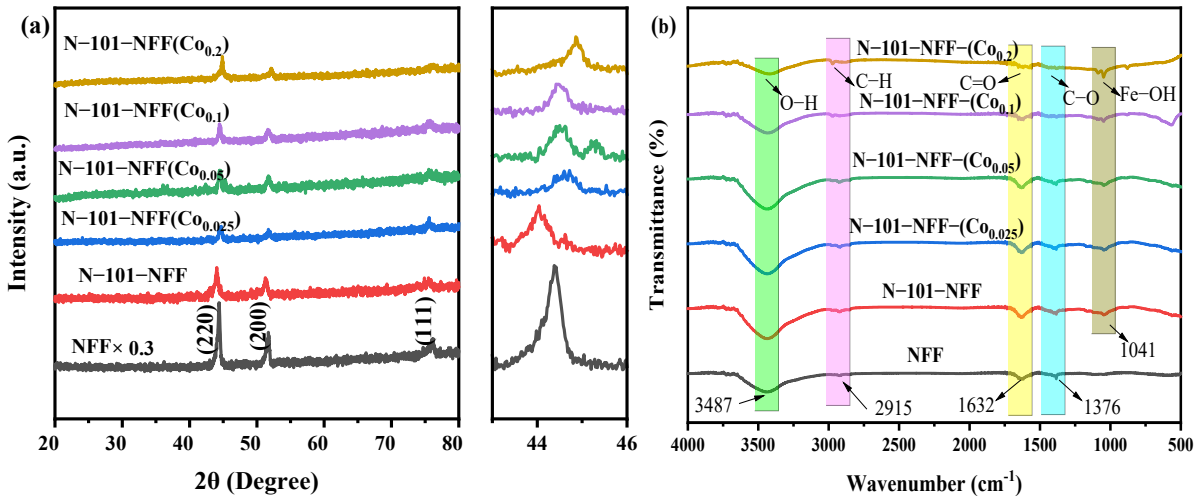


Figure 1. XRD patterns (**a**) and FT-IR spectra (**b**) of NFF, N-101-NFF, N-101-NFF (Co_x).

The functional groups on the catalyst surface were analyzed via FT-IR. As shown in Figure 1b, the band at approximately 3487 cm^{-1} was assigned to the stretching vibration of hydroxyl (OH) groups, the characteristic peak at approximately 2915 cm^{-1} was assigned to the stretching vibration of C-H bonds, the characteristic peak at approximately 1632 cm^{-1} was assigned to the bending vibration of carbonyl (C=O) groups, the characteristic peak at approximately 1376 cm^{-1} corresponded to the stretching vibration of carbon-oxygen (C-O) single bonds, and the characteristic peak at about 1041 cm^{-1} was assigned to the stretching vibration of iron-hydroxyl (Fe-OH) groups [25–29]. The difference in the peaks at approximately 1041 cm^{-1} between N-101-NFF and NFF was mainly derived from the adsorption of molecular water by Fe ion centers; this adsorption phenomenon indirectly confirmed the successful synthesis of MOF-derived materials on the surface of NFF [30,31]. Furthermore, the FT-IR results were consistent with the XRD results, which further confirmed the successful preparation of N-101-NFF (Cox).

2.1.2. SEM and TEM Analysis

The surface morphologies of the materials were observed via SEM, as shown in Figure 2a–c. The NFF has a complex interlaced internal structure and a rough surface. This structural feature provided a favorable foundation for the growth of MOF-derived materials on its surface (Figure 2a). As observed in Figure 2b,c, N-101-NFF and N-101-NFF ($Co_{0.05}$) had rough surfaces with numerous fine particles. These particles exhibited a polyhedral structure similar to that of MIL-101, which was consistent with previous studies [32–34]. Among N-101-NFF and N-101-NFF ($Co_{0.05}$), the nanoparticle size of the latter was larger than that of the former. Additionally, it was observed that the nanoparticles of N-101-NFF agglomerated, while those of N-101-NFF ($Co_{0.05}$) were more uniformly distributed. Notably, this result demonstrated that suitable Co doping could efficiently enhance the dispersibility of the target material.

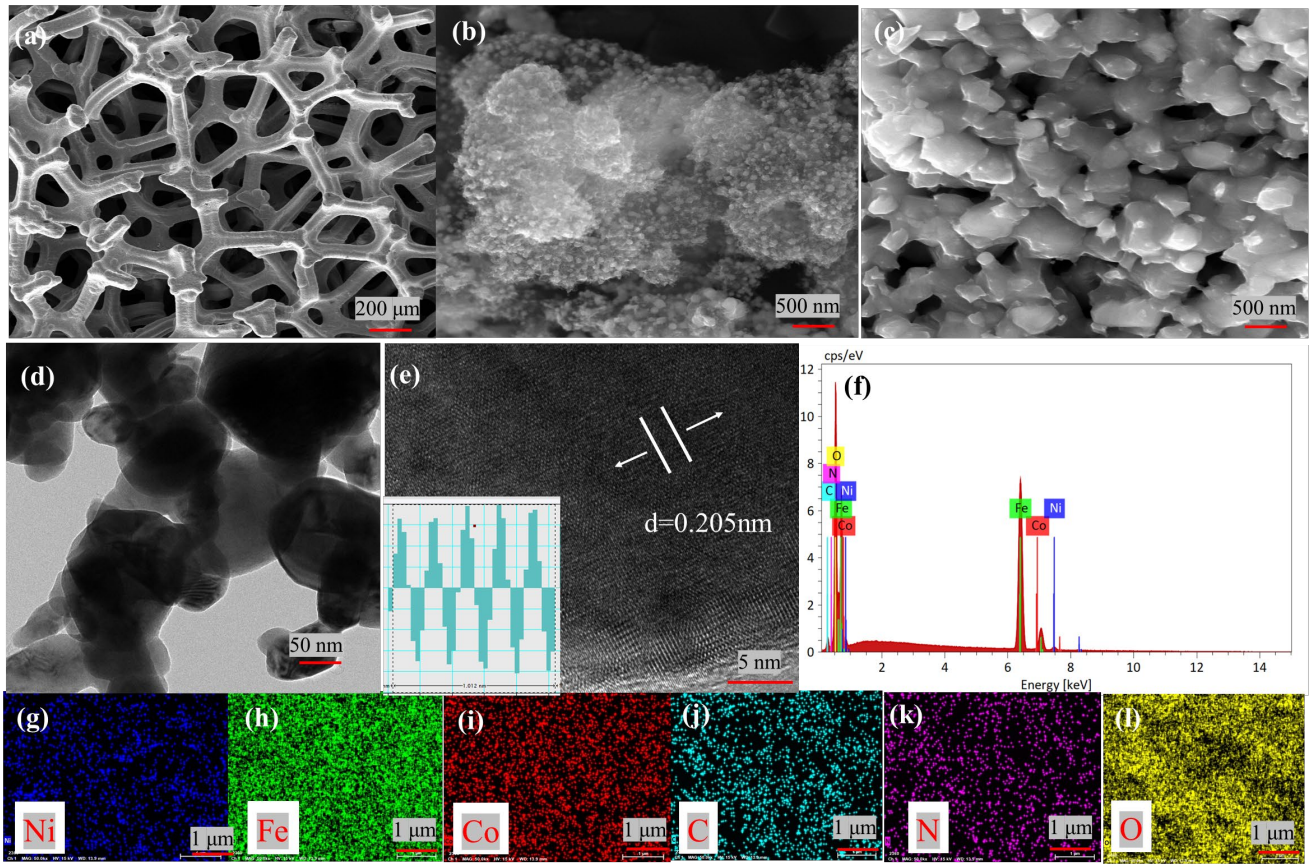


Figure 2. SEM images of NFF (**a**), N-101-NFF (**b**) and N-101-NFF ($Co_{0.05}$) (**c**), N-101-NFF ($Co_{0.05}$) TEM images (**d**), N-101-NFF ($Co_{0.05}$) HRTEM images (**e**), EDS Mapping image (**f**) and EDS elemental mapping images (**g**–**l**) of N-101-NFF ($Co_{0.05}$) SEM.

The TEM image (Figure 2d) clearly revealed the polyhedral structure on the surface of N-101-NFF ($Co_{0.05}$). For these target nanoparticles, the corresponding HRTEM image (Figure 2e) displayed distinct lattice fringes, with an interplanar spacing measured at 0.205 nm. Notably, this interplanar spacing exhibited a slight difference compared to that of N-101-NFF. This difference might be attributed to the doping of Co atoms into the NFF lattice, which modified the lattice spacing of the material. EDS and EDS elemental mapping of N-101-NFF ($Co_{0.05}$) (Figure 2f–i) indicated that the elements on the surface of N-101-NFF included Fe, Ni, Co, C, N, and O, which was consistent with the elemental composition of the material during synthesis. The results from SEM, TEM, and XRD were consistent, further confirming the successful synthesis of N-101-NFF ($Co_{0.05}$).

2.2. Performance Analysis of N-101-NFF ($Co_{0.05}$)

2.2.1. Reaction Parameters

The effects of Co doping ratio, PMS dosage, initial pH value, and humic acid (HA) on CTC degradation were investigated, as presented in Figure 3a–d. The effect of different Co doping ratios on the catalytic degradation of CTC was investigated (Figure 3a). As the Co:Fe molar ratio increased, the catalytic performance of the materials initially improved but later declined. Specifically, the degradation efficiency of N-101-NFF (Cox) was notably higher than that of NFF, with the Co-doped catalysts outperforming the undoped material. Among the Co-doped catalysts, N-101-NFF ($Co_{0.05}$) showed the highest CTC degradation efficiency, increasing from 90.3% to 95.7% compared to N-101-NFF. This improvement indicated that the synergistic effect between Co and Fe enhanced the catalytic performance. Further analysis through pseudo-second-order kinetic fitting (Figure S1) revealed that the rate constants (k) for CTC degradation by N-101-NFF, N-101-NFF ($Co_{0.025}$), N-101-NFF ($Co_{0.05}$), N-101-NFF ($Co_{0.1}$), and N-101-NFF ($Co_{0.2}$) were 0.161, 0.287, 0.396, 0.195, and 0.122 $min^{-1}\cdot L\cdot mg^{-1}$, respectively. This data confirmed that Co doping significantly increased the reaction rate compared to undoped N-101-NFF. The highest rate constant was observed for N-101-NFF ($Co_{0.05}$), indicating that a Co:Fe molar ratio of 0.05:1 was optimal for CTC degradation. On the other hand, excessive Co doping (Co:Fe ratio of 0.2:1) impaired the material's crystallinity, as shown by the XRD results, leading to a decrease in catalytic performance. Therefore, N-101-NFF ($Co_{0.05}$) was selected as the optimal Co-doped catalyst. In addition, the effect of PMS dosage on CTC degradation was assessed (Figure 3b). The degradation efficiency increased gradually with PMS dosage from 0 to 0.08 mmol/L; however, no significant improvement was observed when the dosage exceeded 0.08 mmol/L. This was attributed to the mutual quenching of excessive $SO_4^{\bullet-}$ radicals. Thus, 0.08 mmol/L PMS was selected as the optimal dosage for subsequent experiments. Notably, when the PMS dosage was 0, the concentration of CTC showed little change, suggesting that the adsorption capacity of N-101-NFF ($Co_{0.05}$) for CTC was relatively low.

For catalytic reaction systems, the initial pH of the reaction solution serves as a crucial factor that affects the catalytic performance of the target catalyst. Therefore, to explore the effect of initial pH, the degradation of CTC in the N-101-NFF ($Co_{0.05}$)/PMS system was investigated over a pH range of 3–11. As shown in Figure 3c, this result indicated that the N-101-NFF ($Co_{0.05}$)/PMS system was more suitable for CTC degradation under acidic conditions. This phenomenon might be related to the dissociation constants of CTC, which has three dissociation constants (pKa_1 = 3.3, pKa_2 = 7.4, and pKa_3 = 9.3). When the system pH was lower than pKa_2, CTC existed in protonated ($CTCH_3^+$) and neutral ($CTCH_2$) forms [35]. The electrostatic interaction effectively enhanced the adsorption of CTC and PMS by the catalyst, which facilitated the subsequent activation of PMS for CTC degradation. Furthermore, humic acid (HA) was used as a representative of NOM to evaluate the influence of natural organic matter (NOM) on the N-101-NFF ($Co_{0.05}$)/PMS system (Figure 3d). It could be observed that N-101-NFF ($Co_{0.05}$) maintained the stability of N-101-NFF against NOM interference. When the concentration of HA increased from 0 to 20 mg/L, the CTC degradation efficiency decreased gradually; however, the total decrease was negligible (maximum 11.8%).

Variations in water quality also notably impact the catalyst's catalytic performance. Ultrapure water, tap water, and natural water were used as solvents to prepare CTC solutions and explore the influence of different water matrices on CTC degradation in the N-101-NFF ($Co_{0.05}$)/PMS system. The water quality parameters of various water matrices were summarized in Table S1. As observed in Figure 4a, the CTC degradation efficiency of the N-101-NFF ($Co_{0.05}$)/PMS system was less affected by water matrices, achieving degradation efficiencies of 95.7% (ultrapure water), 89.2% (tap water), and 73.4% (natural water), respectively. This result indicated that N-101-NFF ($Co_{0.05}$) exhibited

favorable anti-interference capability and could adapt to most water qualities. Additionally, the cyclic performance of the N-101-NFF ($Co_{0.05}$)/PMS system was investigated. As shown in Figure 4b, following 5 consecutive cycles, the CTC degradation efficiency of the N-101-NFF ($Co_{0.05}$)/PMS system showed no significant decrease. After the catalytic process, the dissolution of N-101-NFF ($Co_{0.05}$) was assessed using ICP-MS to measure the concentration of dissolved metal ions (such as Fe and Co) after the catalytic reaction. The results showed that the release concentrations of Fe and Co from the N-101-NFF ($Co_{0.05}$) material were 0.43 mg/L and 0.46 mg/L, respectively, which is significantly lower than the maximum allowable discharge concentration of 0.1 mg/L as specified by China's Comprehensive Sewage Discharge Standard (GB8978-1996) [36]. This further confirmed that N-101-NFF ($Co_{0.05}$) exhibited excellent cyclic performance, which demonstrated its potential for practical applications.

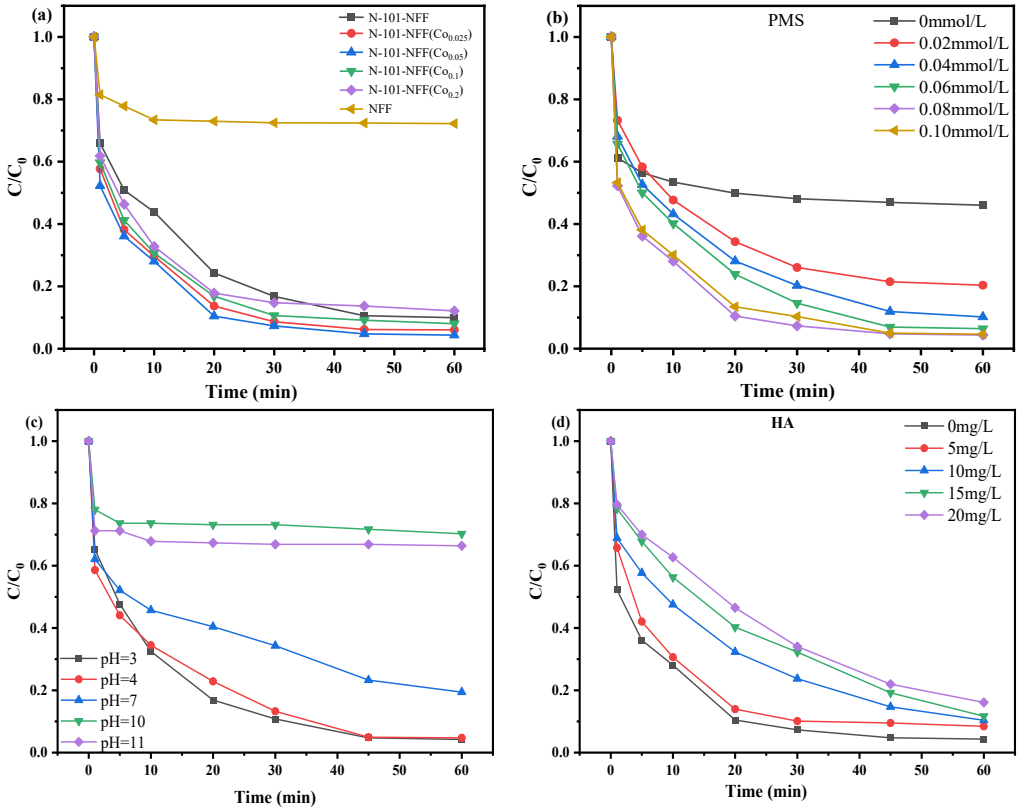


Figure 3. Co doping ratio (**a**), PMS dose (**b**), pH (**c**) and humic acid dose (**d**) on the degradation of CTC (experimental conditions: CTC = 50 mg/L, PMS = 0.08 mmol/L, N-101-NFF ($Co_{0.05}$) = 1 cm^2).

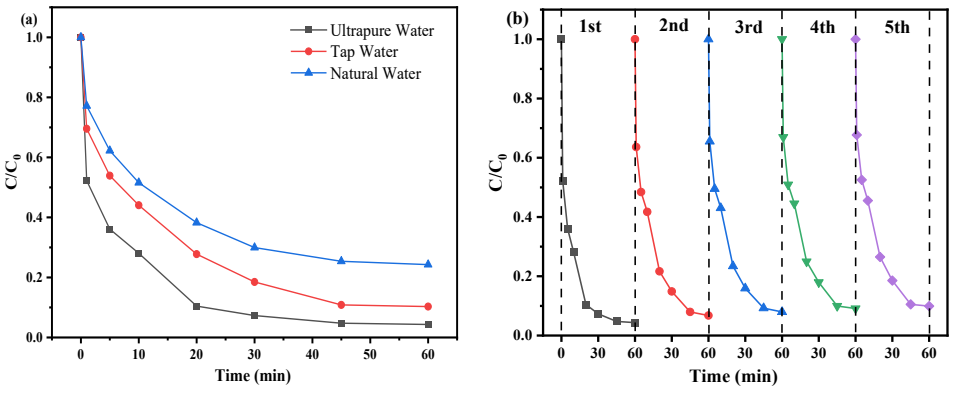


Figure 4. Effect of different water bodies (**a**) and reusability of N-101-NFF ($Co_{0.05}$) (**b**) on CTC degradation (experimental conditions: CTC = 50 mg/L, PMS = 0.08 mM, N-101-NFF ($Co_{0.05}$) = 1 cm^2).

2.2.2. Effects of Reaction Conditions

Natural water inherently contains coexisting anions, and the presence of these anions can affect the stability of the N-101-NFF ($Co_{0.05}$)/PMS catalytic system—consistent with the previously discussed role of anions in interfering with catalytic processes. Additionally, specific anions might even interfere with the PMS activation process, a key step for generating reactive oxidizing species in the N-101-NFF ($Co_{0.05}$)/PMS system, by scavenging $SO_4^{\bullet-}$ and •OH; these two radicals were critical for driving the system's catalytic degradation function [37]. To investigate the effect of different anions on the N-101-NFF ($Co_{0.05}$)/PMS system, this study separately prepared solutions of each anion ($H_2PO_4^-$, SO_4^{2-}, Cl^-, NO_3^-, HCO_3^-, CO_3^{2-}) at concentrations ranging from 0 to 10 mmol/L. As shown in Figure 5a, when $H_2PO_4^-$ was present in the system, the degradation efficiency of CTC by the N-101-NFF ($Co_{0.05}$)/PMS system decreased slightly; when the concentration of $H_2PO_4^-$ was 10 mmol/L, the degradation efficiency decreased by 13.4%. This observation can be attributed to $H_2PO_4^-$ interacting with •OH and $SO_4^{\bullet-}$ in the system, reducing the concentration of free radicals within the system. Furthermore, $H_2PO_4^-$ might also form complexes with divalent metal ions (Fe^{2+}, Ni^{2+}, Co^{2+}) on the catalyst surface, thereby occupying part of the active sites on the catalyst surface [38].

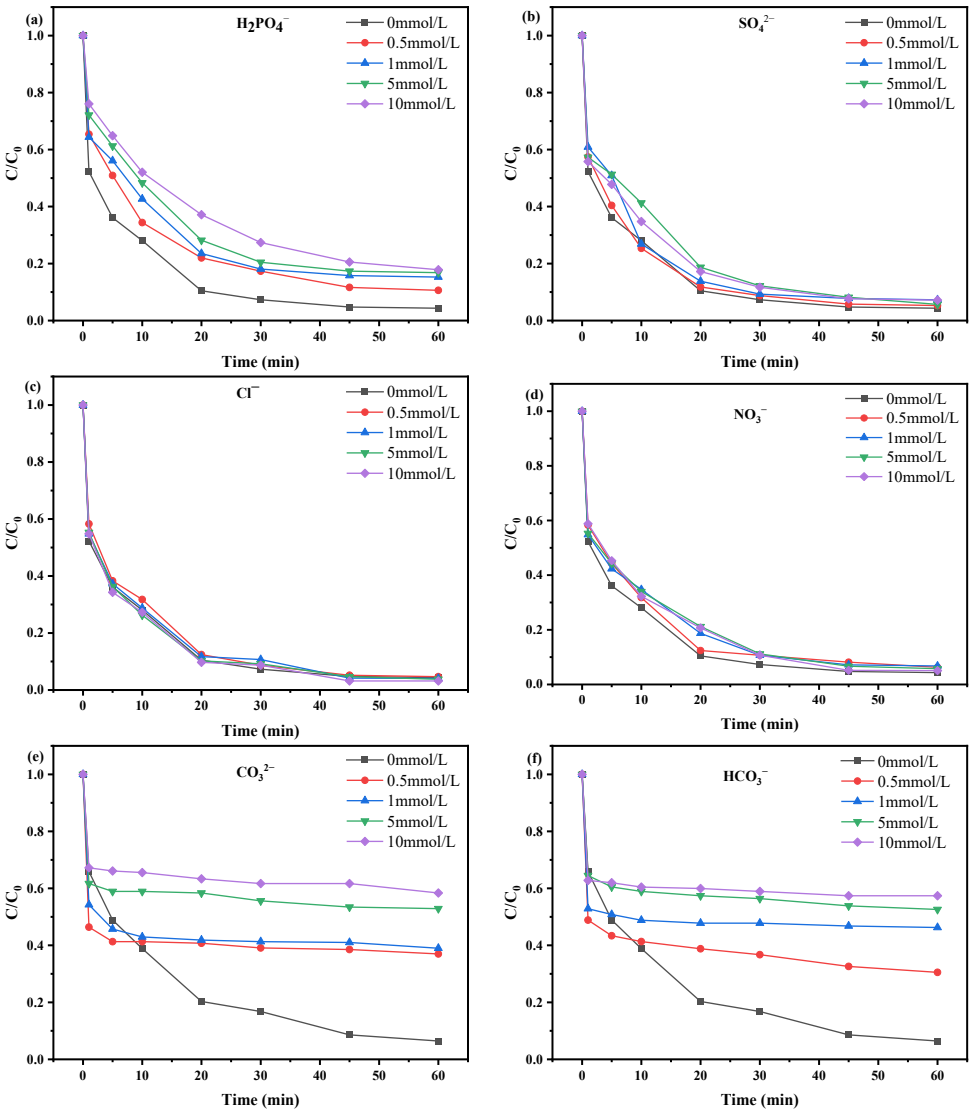


Figure 5. Effects of inorganic ions $H_2PO_4^-$ (**a**), SO_4^{2-} (**b**), Cl^- (**c**), NO_3^- (**d**), CO_3^{2-} (**e**), and HCO_3^- (**f**) on the degradation of chlortetracycline by N-101-NFF ($Co_{0.05}$)/PMS system.

As shown in Figure 5b, SO_4^{2-} exhibited no significant inhibitory effect. When the concentration of SO_4^{2-} reached 10 mmol/L, the CTC degradation efficiency of the N-101-NFF ($Co_{0.05}$)/PMS system decreased by only 2.8%. As presented in Figure 5c, the addition of 0.5 mmol/L Cl^- exerted no significant effect on CTC degradation compared with the blank control group. When the concentration of Cl^- gradually increased to 10 mmol/L, the CTC degradation rate increased to 96.9%. This observation can be ascribed to the reaction of Cl^- with PMS to produce reactive chlorine species (RCS) [39]. As illustrated in Figure 5d, the addition of NO_3^- exerted no significant inhibitory effect on the reaction. Both HCO_3^- and CO_3^{2-} exhibited significant inhibitory effects on the N-101-NFF ($Co_{0.05}$)/PMS system (Figure 5e,f). This finding can be associated with the capacity of HCO_3^- and CO_3^{2-} to interact with $SO_4^{\bullet-}$ and •OH in the system. Furthermore, HCO_3^- and CO_3^{2-} were capable of changing the solution's pH value, a change that might induce the complexation between metal ions and carbonate ions, thereby decreasing the active sites of the catalyst [40,41].

The N-101-NFF ($Co_{0.05}$)/PMS system exhibited favorable resistance to coexisting anions in natural water. Specifically, SO_4^{2-}, Cl^-, and NO_3^- exerted negligible effects on the system for CTC degradation in the N-101-NFF ($Co_{0.05}$)/PMS system. In contrast, $H_2PO_4^-$ slightly reduced the CTC degradation efficiency of the system. Notably, the N-101-NFF ($Co_{0.05}$)/PMS system was primarily affected by HCO_3^- and CO_3^{2-}, which exhibited significant inhibitory effects on CTC degradation.

2.3. Research on Degradation Mechanism

2.3.1. Identification of Active Species

Active species trapping experiments were conducted to identify the key reactive species in the degradation of CTC by the N-101-NFF ($Co_{0.05}$)/PMS system (Figure 6a). Quenchers such as methanol (MeOH), tert-butanol (TBA), L-histidine, p-benzoquinone (p-BQ), silver nitrate ($AgNO_3$), and potassium iodide (KI) were used to target $SO_4^{\bullet-}$/•OH, •OH, $O_2^{\bullet-}$, $^1O_2$, electrons (e^-), and holes (h^+), respectively. The addition of MeOH, TBA, L-histidine, and $AgNO_3$ resulted in a significant reduction in CTC degradation efficiency (by 29–35%), suggesting the involvement of radicals like $SO_4^{\bullet-}$, •OH, $O_2^{\bullet-}$, and e^- in the degradation process [42]. Moreover, p-BQ significantly inhibited CTC degradation, reducing efficiency to 42.7%, indicating the prominent role of $^1O_2$ in the degradation pathway. These results point to a dual mechanism, with the Co-doped N-101-NFF ($Co_{0.05}$)/PMS system notably enhancing the non-radical pathway, primarily dominated by $^1O_2$. This shift in the pathway was primarily attributed to Co incorporation, which enhances the contribution of $^1O_2$ in CTC degradation [43].

In situ EPR spectroscopy was used to analyze the formation and evolution of active species during CTC degradation. Dimethy pyrroline N-oxide (DMPO) and 2,2,6,6-tetramethylpiperidine (TEMP) were employed as spin traps, where DMPO was used to capture $O_2^{\bullet-}$, $SO_4^{\bullet-}$, and •OH, and TEMP was used to trap $^1O_2$.In the N-101-NFF ($Co_{0.05}$)/PMS system (Figure 6b–d), distinct EPR signals of DMPO-•OH, DMPO-$SO_4^{\bullet-}$, DMPO-$O_2^{\bullet-}$ (a 1:1:1:1 quartet signal), and TEMP-$^1O_2$ were observed. The intensity of these EPR signals increased with the extension of the catalytic reaction time. Among these signals, the intensity of the DMPO-•OH signal was much higher than that of the DMPO-$SO_4^{\bullet-}$ signal. This phenomenon might be attributed to the rapid conversion of DMPO-$SO_4^{\bullet-}$ to DMPO-•OH (a known conversion behavior in aqueous systems). In conclusion, the formation of $O_2^{\bullet-}$, $SO_4^{\bullet-}$, and •OH indicates that the CTC degradation process relies on a radical pathway; meanwhile, the presence of $^1O_2$ further confirmed that a non-radical pathway also exists simultaneously for CTC degradation in this catalytic system.

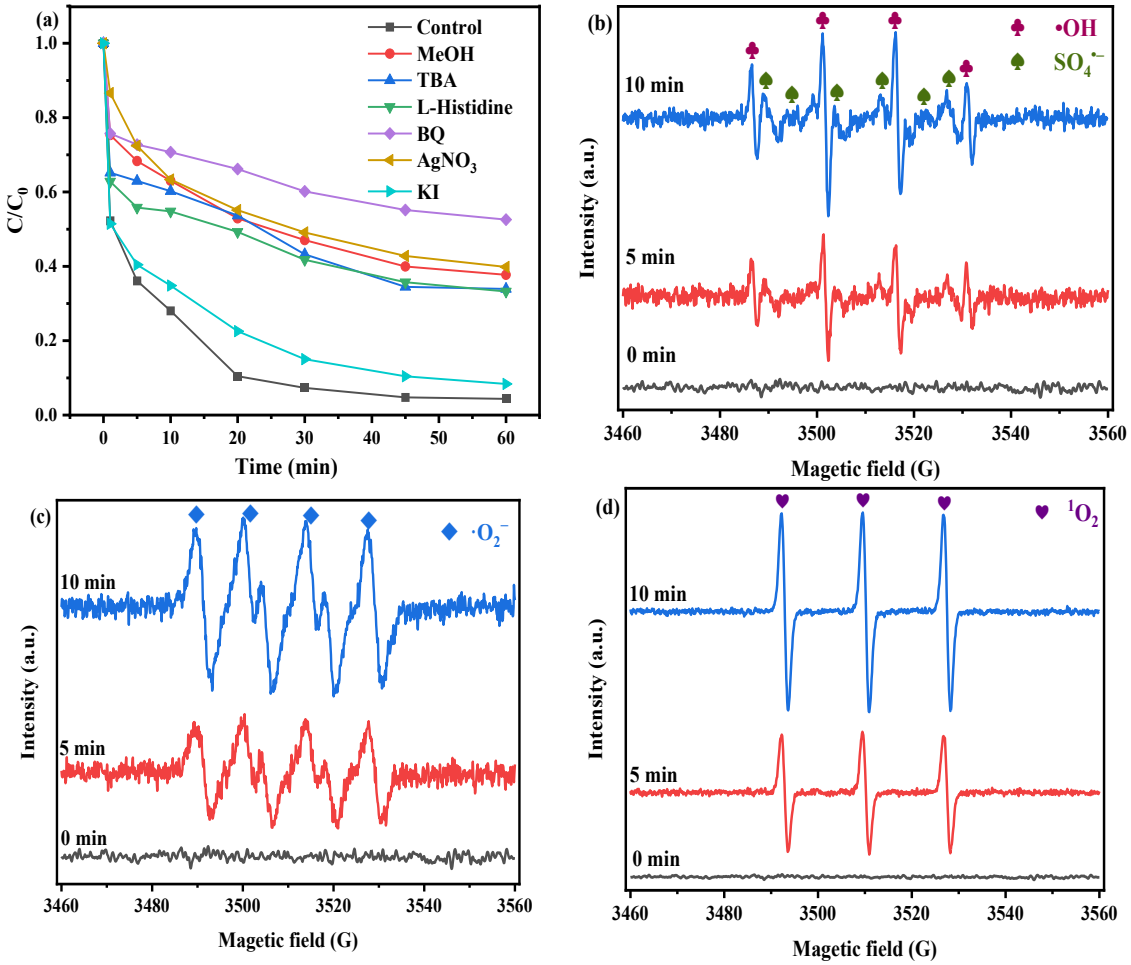


Figure 6. Radical trapping experiments of N-101-NFF ($Co_{0.05}$)/PMS system (**a**), DMPO spin-trapping EPR spectra for •OH, $SO_4^{\bullet-}$ and $O_2^{\bullet-}$, respectively (**b**,**c**), and TEMP spin-trapping EPR spectra for $^1O_2$ (**d**).

2.3.2. Electronic Transfer Mechanism

The electrochemical properties of N-101-NFF (Co_x) were explored via electrochemical measurement techniques. Cyclic voltammetry (CV) curves of the various catalysts are presented in Figure 7a. The integral area of CV curves reflects the redox capacity of the catalysts. Significantly, the redox peaks in the CV curve of N-101-NFF ($Co_{0.05}$) are associated with the redox transitions of Co^{2+}/Co^{3+} at approximately 1.45 V and as well as Ni^{2+}/Ni^{3+} at around 1.4 V [44], which are consistent with the reported redox potentials for these transitions. The observed high current density and significant redox capacity of N-101-NFF ($Co_{0.05}$) highlight the enhancement in electron transfer due to Co doping [45]. This enhanced electron transfer promotes the activation of PMS, thereby facilitating the degradation of pollutants, such as CTC. Linear sweep voltammetry (LSV) curves (Figure 7b) and chronoamperometry (i-t) curves (Figure 7c) demonstrated that when PMS, CTC, and N-101-NFF ($Co_{0.05}$) came into contact, the current density decreased. Concurrently, instantaneous electron transfer took place between the surface of N-101-NFF ($Co_{0.05}$) and the surfaces of PMS and CTC molecules [46].

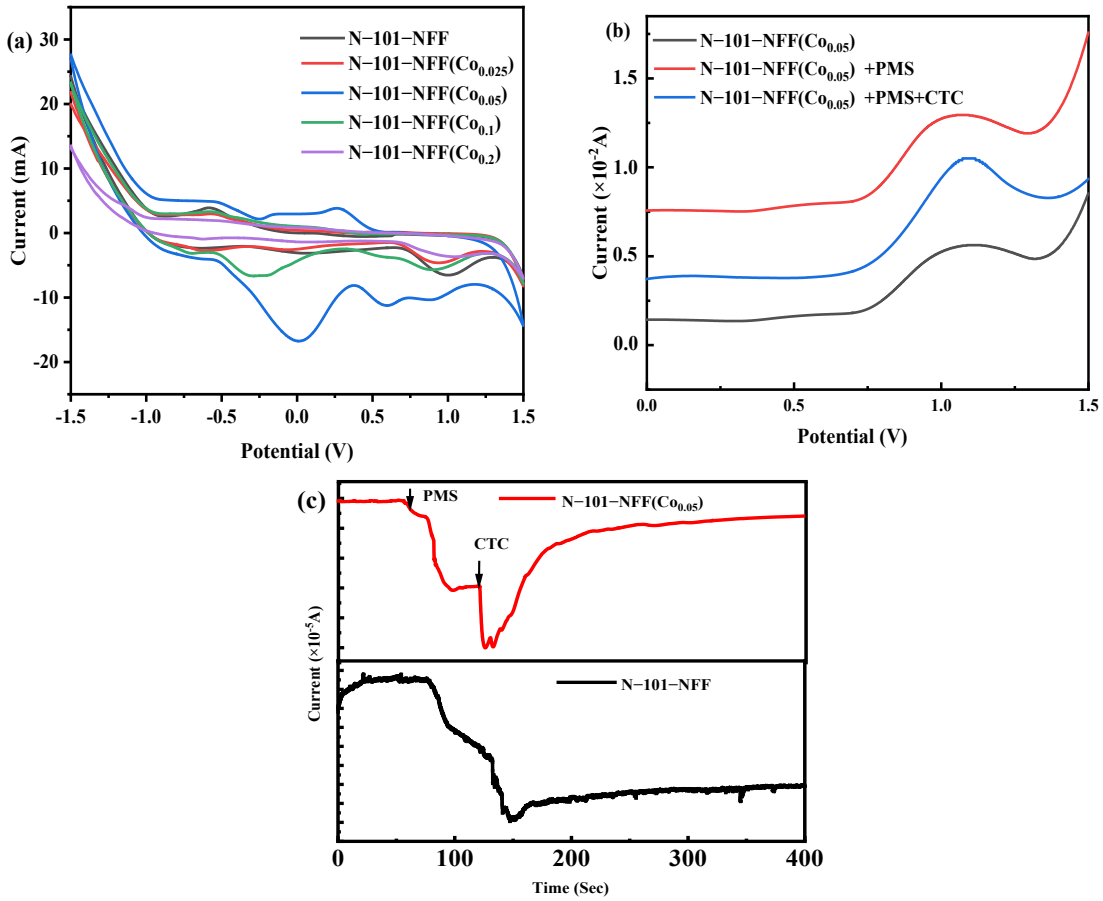


Figure 7. CV curves (**a**) of N-101-NFF and N-101-NFF (Co_x), LSV curve (**b**) of N-101-NFF (Co_x), and it curves of N-101-NFF and N-101-NFF (Co_x) (**c**).

2.3.3. Characterization of Catalyst After Reaction

To conduct an in-depth study on the surface element distribution and active components of the catalyst before and after the reaction, XPS characterization was performed on the catalyst before and after the reaction, with the results shown in Figure 8a–f. The contents of various active components on the catalyst surface before and after the reaction are presented in Table S2. The high-resolution XPS spectrum of Fe 2p (Figure 8a) can be deconvoluted into Fe^{2+} species (binding energies: 710.9 eV, 723.4 eV), Fe^{3+} species (binding energies: 713.8 eV, 726.9 eV), and Fe^0 (binding energies: 707.5 eV, 721.3 eV). Compared with the contents of various valence species of Fe in the N-101-NFF ($Co_{0.05}$) catalyst before the reaction, after the reaction, the ratio of Fe^{2+} to Fe^{3+} decreased from 1.64 to 1.43, while the proportion of Fe^0 was reduced from 0.96 to 0.61. The high-resolution XPS spectrum of Ni 2p was shown in Figure 8b, after the catalytic reaction, the ratio of Ni^{2+} to Ni^{3+} decreased from 1.03 to 0.93, while the proportion of Ni^0 increased from 0.24 to 0.45. The high-resolution XPS spectrum of Co 2p is shown in Figure 8c, where the characteristic peaks at 781.6 eV and 788.9 eV both correspond to Co^{2+} species. Comparing the valence distribution of Co in the N-101-NFF ($Co_{0.05}$) catalyst before and after the reaction, after the reaction, the ratio of Co^{2+} to Co^{3+} increased from 0.66 to 0.98. During the PMS activation process, the active intermediate Fe^{2+}/Ni^{3+} species play a crucial role. Subsequently, Fe^{3+}/Ni^{3+} react with HSO_5^- to generate $SO4^{\bullet-}$, while the reaction between Fe/Ni species and Fe^{3+}/Ni^{3+} accomplishes the redox cycling of Fe/Ni. Furthermore, Co^{2+}/Co^{3+} react with HSO_5^- to produce $SO_4^{\bullet-}$; additionally, Ni^0/Fe^0 react with Co^{3+} to form $Fe^{2+}/Ni^{2+}/Co^{2+}$. These

results demonstrate that the Fe^{2+}/Fe^{3+}, Ni^{2+}/Ni^{3+}, and Co^{2+}/Co^{3+}, as well as Fe^0 and Ni^0, are all involved in the redox reactions during the catalytic process.

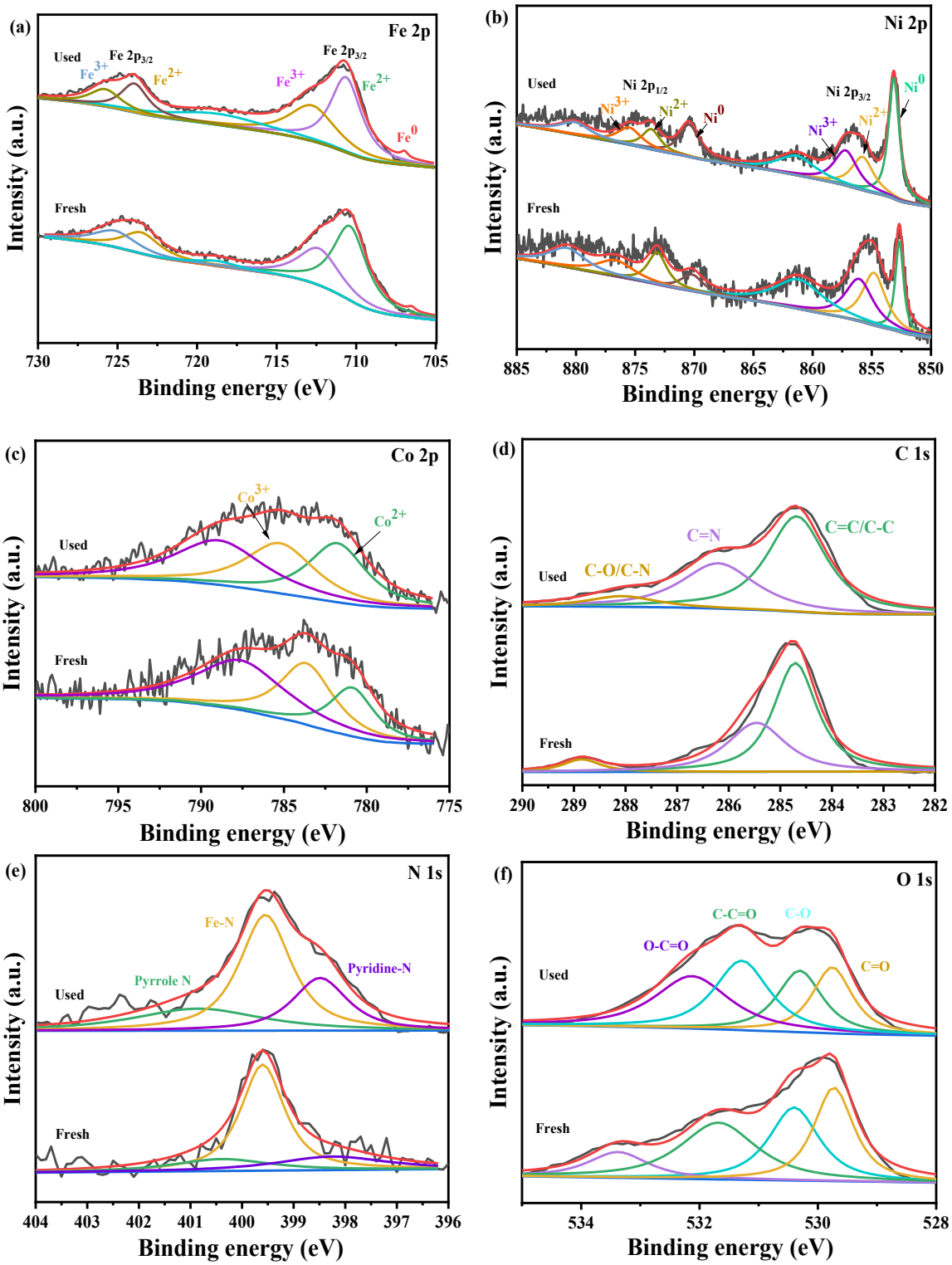


Figure 8. XPS spectra of fresh and used N-101-NFF ($Co_{0.05}$): Fe 2p (**a**), Ni 2p (**b**), Co 2p (**c**), C 1s (**d**), N 1s (**e**), and O 1s (**f**).

The high-resolution XPS spectrum of C 1s is shown in Figure 8d, where the characteristic peak at 286.21 eV corresponded to the C=N group. Electron-rich C=N groups act as active sites to activate PMS [47,48]. The high-resolution XPS spectrum of N 1s

(Figure 8e) can be deconvoluted into three characteristic peaks: pyridinic N (binding energy: 398.42 eV), Fe-N bonds (binding energy: 399.53 eV), and pyrrolic N (binding energy: 401.28 eV) [49,50]. Pyridinic N and pyrrolic N can effectively activate PMS by anchoring iron atoms, thereby generating ·OH and $SO_4^{\bullet-}$ [51–53]. Furthermore, the presence of Fe-N bonds can effectively promote the adsorption of chlorinated hydrocarbon contaminants (CTC) by the material; meanwhile, due to the electronegativity difference between Fe and N, they can also significantly enhance the electron transfer rate of the material. The high-resolution XPS spectrum of O 1s (Figure 8f) can be deconvoluted into four characteristic peaks: C=O (binding energy: 529.64 eV), C-O (binding energy: 530.32 eV), C-C=O (binding energy: 531.34 eV), and O-C=O (binding energy: 532.13 eV) [54]. After the reaction, the post-reaction C=O/C-O ratio decreased from 1.02 to 0.95, which indicated that C=O groups can effectively participate in the redox reactions during the catalytic process [55,56].

2.3.4. Catalytic Reaction Mechanism

Based on the previous experimental findings, this study proposes the degradation mechanism of CTC in the N-101-NFF ($Co_{0.05}$)/PMS system (Figure 9).

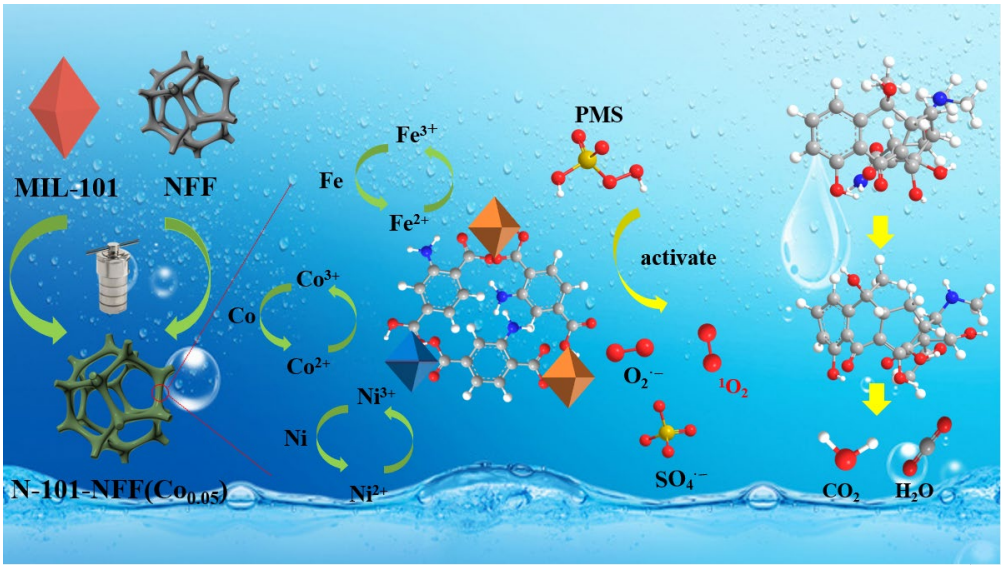


Figure 9. Mechanism diagram of N-101-NFF ($Co_{0.05}$)/PMS system for degradation of CTC.

For the radical pathway, PMS can react with zero-valent metals in N-101-NFF ($Co_{0.05}$), generating $SO_4^{\bullet-}$ via electron transfer. Fe^{2+}/Ni^{2+} and Co^{2+} on the catalyst surface can also effectively activate PMS, generating $SO_4^{\bullet-}$ and hydroxide ions (OH^-). $SO_4^{\bullet-}$ has poor stability; once generated, it reacts rapidly with water molecules in the system and converts into ·OH. Fe^{3+}/Ni^{3+}/Co^{2+} on the catalyst surface can react with PMS, first generating peroxymono $SO_5^{\bullet-}$, and then further generating $SO_4^{\bullet-}$. Furthermore, the products from the spontaneous hydrolysis of PMS in the system reacted with ·OH generated previously, producing superoxide anion radicals ($O_2^{\bullet-}$) and hydrogen ions(H^+). The presence of zero-valent metals in N-101-NFF ($Co_{0.05}$) can effectively improve the valence cycling efficiency of Fe^{3+}/Ni^{3+}/Co^{3+}/Fe^{2+}/Ni^{2+}/Co^{2+}, thereby enhancing the PMS activation efficiency.

For the non-radical pathway, the peroxymonosulfate radical $SO_5^{\bullet-}$, a product of the reaction between Fe^{3+}/Ni^{3+}/Co^{3+} on the catalyst surface and PMS, reacts further with water molecules in the system to generate $^1O_2$. Furthermore, $SO_5^{\bullet-}$ can also react with Fe^{3+}/Ni^{3+}/Co^{3+} on the catalyst surface to generate $^1O_2$. The self-decomposition of PMS can also generate a small amount of $^1O_2$. The superoxide anion radicals ($O_2^{\bullet-}$) and hydrogen ions (H^+) generated previously can also react further to generate $^1O_2$. Furthermore, the

zero-valent metals in N-101-NFF ($Co_{0.05}$) can effectively utilize dissolved oxygen (DO) in the solution to generate $^1O_2$, and this DO-dependent pathway is also one of the main pathways for $^1O_2$ generation. As active sites capable of catalyzing the activation of PMS, C=O groups coucanld activate PMS to generate sulfate ions (SO_4^{2-}) and $^1O_2$.

In summary, the degradation of CTC in the N-101-NFF ($Co_{0.05}$)/PMS system followed a combined radical and non-radical pathway, in which $^1O_2$ played a dominant role. Compared with the N-101-NFF/PMS system, the role of $^1O_2$ was significantly enhanced, which could be attributed to the significant increase in the content of zero-valent metals and C=O groups in N-101-NFF ($Co_{0.05}$) compared with N-101-NFF; this changes further improved the utilization efficiency of dissolved oxygen in the N-101-NFF ($Co_{0.05}$)/PMS system, ultimately promoting $^1O_2$ production.

2.4. Degradation Pathway and Toxicity Assessment

2.4.1. Degradation Pathway of CTC

To better reveal the catalytic degradation process of CTC by N-101-NFF ($Co_{0.05}$), this study identified the degradation intermediates of CTC using high-performance liquid chromatography–mass spectrometry (HPLC-MS), and the results are presented in Table S3 and Figure 10.

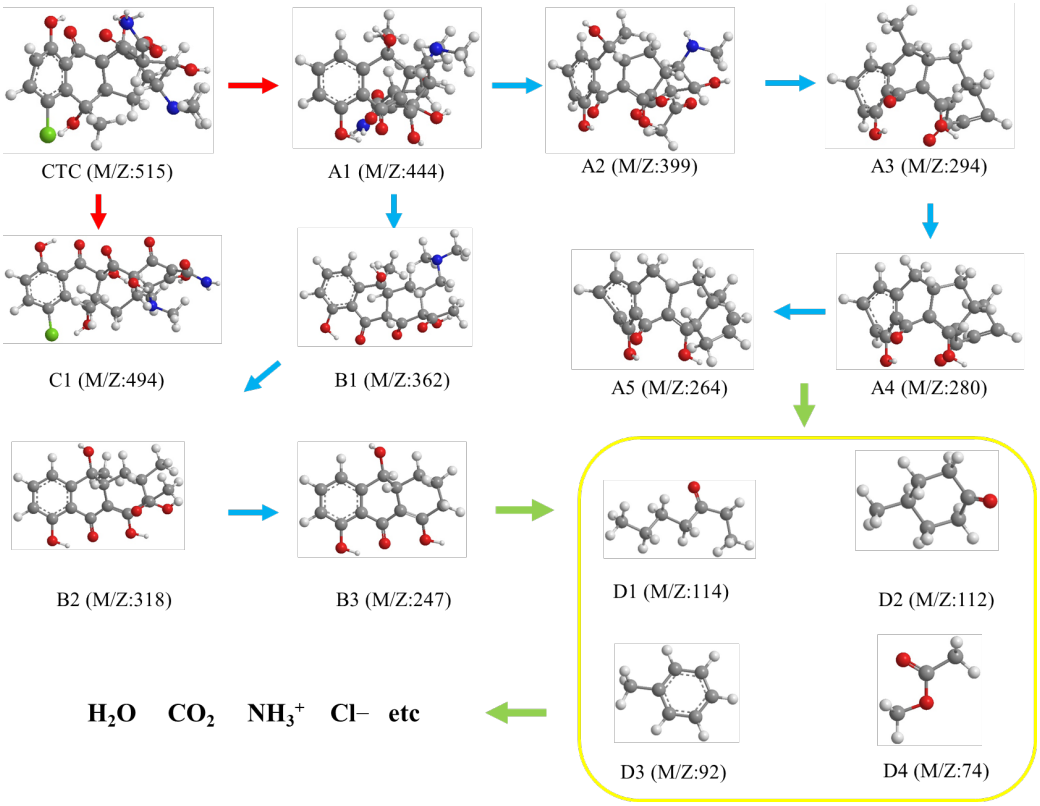


Figure 10. Possible degradation path of CTC in N-101-NFF ($Co_{0.05}$)/PMS system.

Based on the obtained mass spectrometry information, this study can classify the degradation pathways of CTC into three main routes. The main intermediate A1 with m/z = 444 corresponds to the product of CTC (m/z = 515) after simultaneous removal of one HCl molecule (i.e., loss of one Cl^- and one H^+) under the action of ·OH and $SO_4^{\bullet-}$ [57]. Intermediate A3 (m/z = 399) in Route 1 was formed from the main intermediate A1 via demethylation and deamination [58]. Route 2 represents the main difference in degradation pathways between the current system (N-101-NFF ($Co_{0.05}$)/PMS) and the N-101-NFF/PMS

system, which can be attributed to the doping of Co enhancing the role of the non-radical pathway dominated by $^1O_2$. The main intermediate A1 was further converted to intermediate B1 (m/z = 362) under the action of $^1O_2$, and then formed an intermediate with m/z = 318 through the cleavage of the C-N$(CH_3)_2$ bond [59]. Intermediate C1(m/z = 494) in Route 3 corresponded to the product of CTC, after combining with one oxygen atom (i.e., oxygenation reaction) and removing one HCl molecule [60,61]. Other intermediates could also be generated through a series of reactions, including demethylation, deamination, decarbonylation (accompanied by double bond cleavage), hydroxyl substitution or elimination, and ring-opening processes. These reactions collectively contributed to the formation of diverse intermediate species during the degradation process [62,63]. During the degradation process, these intermediates can be further oxidized in subsequent steps and eventually were transformed into CO_2, H_2O, and simple inorganic ions—representing the final mineralization products of the reaction.

2.4.2. Toxicity Analysis

The intermediates generated during CTC degradation may pose ecological risks. Therefore, this study used the toxicity assessment software T.E.S.T. (5.1.2) (Toxicity Estimation Software Tool) to evaluate the toxicity of these intermediates, and the selected assessment indicators include four key toxicological parameters: acute toxicity (LC_{50}, median lethal concentration), bioconcentration factor, developmental toxicity, and mutagenicity. Detailed data are presented in Table S3. As shown in Figure 11a, only a few intermediates have slightly higher acute toxicity than CTC, while the acute toxicity of the remaining intermediates was reduced, and some even see their acute toxicity decrease to a non-toxic level.

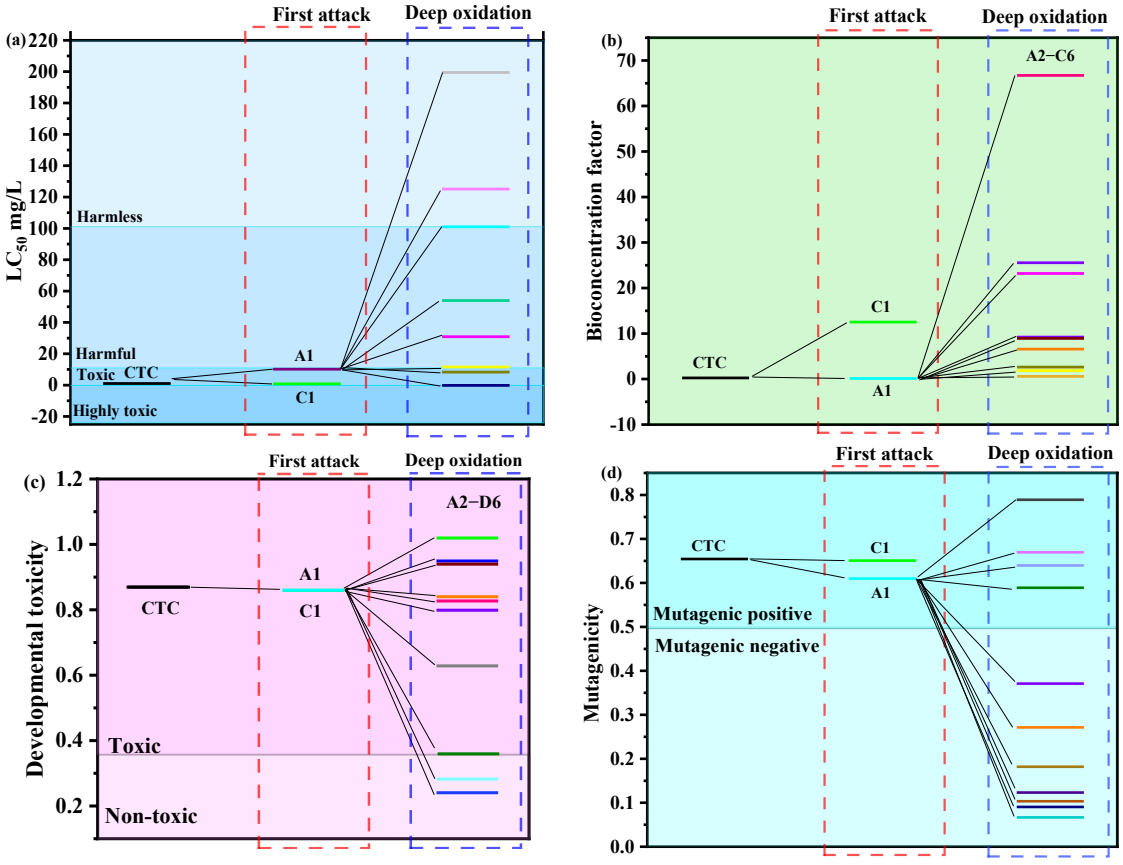


Figure 11. Acute toxicity (**a**), bioaccumulation factor (**b**), developmental toxicity (**c**), and mutagenicity (**d**) of CTC and intermediates in N-101-NFF ($Co_{0.05}$)/PMS system.

Figure 11b presents a comparison of the bioconcentration factors (BCF) between CTC and its intermediates. The results show that most intermediates have an increased BCF, which may enhance their environmental enrichment risk. The developmental toxicity of CTC and its intermediates is shown in Figure 11c. Most intermediates exhibit reduced developmental toxicity, and some even decrease to a non-toxic level. The mutagenicity data of CTC and its intermediates are shown in Figure 11d. Most intermediates have lower mutagenicity than CTC. Furthermore, compared with the N-101-NFF/PMS system, the N-101-NFF ($Co_{0.05}$)/PMS system has significantly lower overall mutagenicity, and more intermediates show negative mutagenicity; this indicates that Co doping was more conducive to degrading CTC into less toxic products. Based on the above findings, although the intermediates of CTC degradation have increased BCFs, their acute toxicity, developmental toxicity, and mutagenicity were significantly reduced. This confirms that the N-101-NFF ($Co_{0.05}$)/PMS system is a relatively environmentally friendly system for CTC degradation.

3. Materials and Methods

3.1. Chemicals and Materials

Nickel–iron foam (NFF with a dimension of 10 mm × 10 mm × 1.5 mm) was purchased from Jiang Su Kunshan Xingzhenghong Electronic Materials Co., Ltd. Aminoterephthalic acid (NH_2-H_2BDC), dimethylformamide (DMF), iron(III) chloride hexahydrate ($FeCl_3 \cdot 6H_2O$), cobalt(II) chloride hexahydrate ($CoCl_2 \cdot 6H_2O$), potassium chloride (KCl), anhydrous methanol (MeOH), nitric acid (HNO_3), ssulfuric acid (H_2SO_4), sodium hydroxide (NaOH), silver nitrate ($AgNO_3$), potassium bromide (KBr), and tert-butanol (TBA) were all purchased from Shang Hai Sinopharm Chemical Reagent Co., Ltd. PMS and CTC were acquired from Aladdin Reagent Co., Ltd. (Shanghai, China). All chemicals used in the present study met analytical grade standards and were used directly without further purification; ultrapure water was consistently used throughout the experiment.

3.2. Preparation of Catalyst

3.2.1. Pretreatment of Nickel–Iron Foam

NFF with a dimension of 10 mm × 10 mm × 1.5 mm was immersed in a hydrochloric acid solution (4 mol/L, of analytical grade), followed by ultrasonic cleaning (frequency: 40 kHz; power: 150 W) for 3 min to etch the surface oxide layer. Subsequently, the NFF was sequentially subjected to ultrasonic cleaning (same parameters as above: 40 kHz, 150 W) in ethanol solution (95% v/v, analytical grade) and distilled water (DW) for 3 min each. Finally, the cleaned NFF substrate was dried in a forced-air oven at 60 °C for 2 h; this drying step specifically targets the removal of residual solvents—ethanol and distilled water—that adhere to its surface, ensuring no solvent residues remain for subsequent experiments.

3.2.2. Preparation of N-101-NFF (Co_x)

Solution A was prepared by dissolving 5 mmol of 2-aminoterephthalic acid (NH_2-H_2BDC, AR) in 30 mL of N, N-dimethylformamide (DMF, AR). Solution B was prepared by dissolving 10 mmol of iron (III) chloride hexahydrate ($FeCl_3 \cdot 6H_2O$, AR) and varying amounts of cobalt (III) chloride hexahydrate ($CoCl_3 \cdot 6H_2O$, AR) (0.25 mmol, 0.5 mmol, 1 mmol, 2 mmol) in 30 mL of DMF. Solutions A and B were stirred separately until all solutes fully dissolved. After full dissolution, solutions A and B were mixed, and the cleaned NFF was then added to the mixture. After thorough stirring, the mixture was transferred to a stainless-steel autoclave equipped with a Teflon liner. Subsequently, the autoclave was placed in a forced-air oven and heated at 110 °C for 24 h. After the reaction, the obtained product was rinsed sequentially with ethanol (95%, AR) and deionized water (DI water), followed by drying overnight in a forced-air oven at 60 °C. Finally, the dried

product was calcined in a tube furnace at a heating rate of 5 °C/min, with the temperature maintained at 700 °C for 3 h, yielding the N-101-NFF (Co_x) material. Here, "x" represents the molar ratio of doped Co to Fe, with values of 0.025, 0.05, 0.1, and 0.2, corresponding to the Co dosages of 0.25 mmol, 0.5 mmol, 1 mmol, and 2 mmol, respectively. The preparation process of N-101-NFF (Co_x) is illustrated in Figure 12.

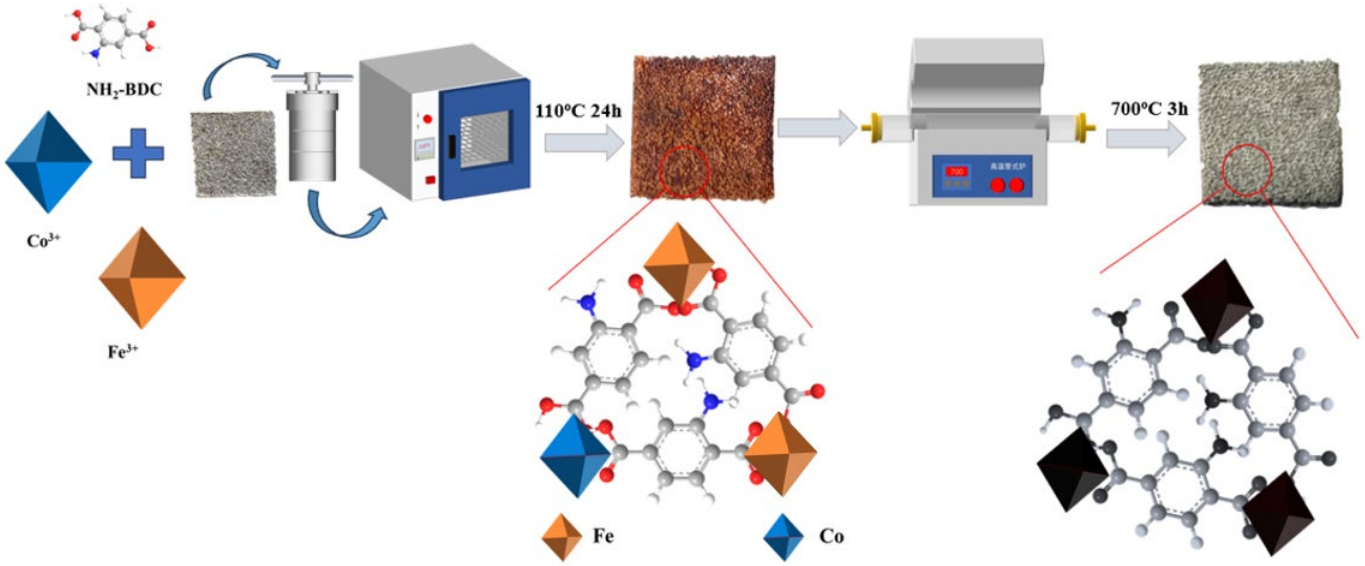


Figure 12. The synthesis process of N-101-NFF (Co_x).

3.3. Characterization and Degradation Experiments

The prepared materials were characterized by X-ray diffraction (XRD), Fourier Transform Infrared Spectroscopy (FT-IR), Scanning Electron Microscope (SEM) equipped with an Energy Dispersive X-ray Spectrometer (EDX), Energy Dispersive Spectroscopy (EDS), Transmission Electron Microscopy (TEM), High-Resolution Transmission Electron Microscopy (HRTEM), electron paramagnetic resonance (EPR) technologies, high-performance liquid chromatography–mass spectrometry (HPLC-MS) and X-ray photoelectron spectroscopy (XPS). The characterization parameters and instruments are shown in Text S1.

All degradation tests were conducted as follows: 50 mL of a 50 mg/L chlortetracycline (CTC) solution, a specific dose of the catalyst, and a specific dose of PMS were added to an Erlenmeyer flask. After thorough mixing, the mixture was placed on a shaker and shaken. Several sampling time points were established. At each time point, 1 mL of the reaction solution was sampled with a syringe, followed by filtration through a 0.22 μm polyethersulfone (PES) syringe filter. Following a 5-fold dilution of the filtrate, a UV-Vis (ultraviolet–visible) spectrophotometer was used to determine the concentration of CTC at a wavelength of 365 nm.

4. Fixed Bed Application of the System

To further explore the practical application potential of N-101-NFF ($Co_{0.05}$), this study constructed a fixed-bed reactor, filled it with the catalyst, and investigated its degradation performance for the continuous flow of CTC-contaminated water (Figure 13a). The flow rates of the CTC solution and PMS solution were set to 0.2 $L \cdot h^{-1}$ and 200 $\mu L \cdot h^{-1}$, respectively. The packing amount of N-101-NFF ($Co_{0.05}$) was 100 cm^2. (Note: Catalyst packing amount was typically measured by volume (cm^3) or mass (mg/g). If "cm^2" was a typo, it was recommended to correct it to cm^3 or mg to ensure the physical meaning of the experimental data is accurate.) As shown in Figure 13b, during 24 h of continuous

operation, the CTC removal rate was consistently maintained above 90.5%. Although the removal efficiency decreases slightly compared with the reactor's initial operation stage, the decline range was small. This indicated that N-101-NFF ($Co_{0.05}$) could maintain excellent degradation performance during long-term continuous operation, which further confirms its application potential in actual wastewater treatment scenarios. Compared with N-101-NFF, N-101-NFF ($Co_{0.05}$) exhibited superior catalytic activity, with a smaller performance decay range during operation, demonstrating better operational stability and recycling performance.

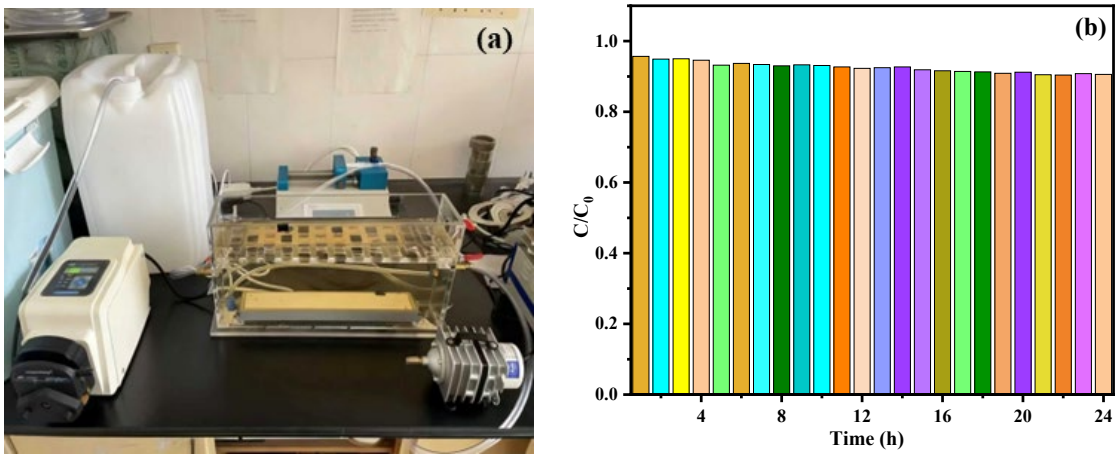


Figure 13. Fixed-bed performance of N-101-NFF ($Co_{0.05}$)/PMS system (**a**) and its CTC degradation performance (**b**) (CTC flow rate = 200 mL/h, PMS flow rate = 200 μL/h, N-101-NFF ($Co_{0.05}$) =100 cm^2).

5. Conclusions

In summary, on the basis of N-101-NFF, we successfully synthesized N-101-NFF (Co_x) by introducing a cobalt (Co) source and realized efficient activation of PMS for the degradation of CTC. Co doping effectively enhanced the dispersion of the material and improved the metal synergistic effect in the catalyst, thereby promoting interfacial electron transfer, PMS decomposition, and the generation of active species. Through active species quenching experiments and EPR analysis, it was confirmed that CTC degradation in the system proceeded via both radical pathways (characterized by $SO_4^{\bullet-}$ and •OH) and non-radical pathways (dominated by $^1O_2$), with $^1O_2$ identified as the primary active species. Combined LC-MS and T.E.S.T. analysis of CTC intermediates demonstrated that Co doping significantly reduced the mutagenicity of these intermediates. Therefore, the N-101-NFF ($Co_{0.05}$)/PMS system enabled efficient and safe CTC degradation. This system addressed the drawbacks of traditional powdered iron-based catalysts and laid a technical foundation for the development of high-efficiency persulfate-activating catalysts.

Supplementary Materials: The following supporting information can be downloaded at https://www.mdpi.com/article/10.3390/catal16010039/s1, Text S1: Characterization technique; Table S1: Parameters of water matrixes; Table S2: Composition of N-101-NFF (Co0.05) surface elements and functional groups before and after reaction; Table S3: Ecotoxicity of CTC and its intermediates; Figure S1: Second-order kinetic constants of CTC degradation.

Author Contributions: Conceptualization, Y.Y. and X.Z.; methodology, Y.Y.; validation, X.G. and J.H.; formal analysis, M.C., L.Q. and L.Y.; writing—original draft preparation, Y.Y.; writing—review and editing, Y.Y. and X.G.; supervision, X.Z.; funding acquisition, Y.Y. and X.Z. All authors have read and agreed to the published version of the manuscript.

Funding: This work is sponsored financially by the National Natural Science Foundation of China (Nos. 12075147, 42177405) and Natural Science Foundation of Shanghai (22ZR144430).

Data Availability Statement: The authors declare that all data supporting the findings of this study are available within the article.

Conflicts of Interest: The authors declare no conflicts of interest.

References

1. Hain, E.; Adejumo, H.; Anger, B.; Orenstein, J.; Blaney, L. Advances in antimicrobial activity analysis of fluoroquinolone, macrolide, sulfonamide, and tetracycline antibiotics for environmental applications through improved bacteria selection. *J. Hazard. Mater.* **2021**, *415*, 125686. [CrossRef] [PubMed]
2. Li, Z.; Liu, R.; Gao, W.; Zhang, W.; Li, C.; Liu, X.; Wang, N. $CuFe_2O_4$/penicillin residue biochar heterogeneous Fenton-like catalyst used in the treatment of antibiotic wastewater: Synthesis, performance and working mechanism. *J. Water Process. Eng.* **2023**, *55*, 104124. [CrossRef]
3. Jing, L.; Liu, S.; Wang, T.; Zhang, Z.; Zhao, X.; Sun, Z.; Hao, P.; Hu, Y.; Yang, W.; Quan, R.; et al. MOF derived highly dispersed bimetallic Fe-Ni nitrogen-doped carbon for enhanced peroxymonosulfate activation and tetracycline degradation. *J. Environ. Chem. Eng.* **2024**, *12*, 112470. [CrossRef]
4. Wu, J.-X.; Mao, Y.; Zhou, Y.; Wang, Z.; Wei, S.; Cowie, B.C.; Marshall, A.T.; Wang, Z.; Waterhouse, G.I. Divalent site doping of NiFe-layered double hydroxide anode catalysts for enhanced anion-exchange membrane water electrolysis. *Chem. Eng. J.* **2025**, *508*, 160753. [CrossRef]
5. Liu, N.; Tian, M.; Zhang, Y.; Yang, J.; Wang, Z.; Dai, W.; Quan, G.; Lei, J.; Zhang, X.; Tang, L. Three-dimensional MIL-88A(Fe)-derived α-Fe_2O_3 and graphene composite for efficient photo-Fenton-like degradation of ciprofloxacin. *Chin. Chem. Lett.* **2025**, *36*, 111063. [CrossRef]
6. Yang, Y.; Yang, B.; Gao, X.; Dang, X.; Jin, Z.; Zhang, X. MOF-on-MOF composite material derived from ZIF-67 precursor activated by peroxymonosulfate for the removal of metronidazole. *J. Water Process. Eng.* **2025**, *72*, 107467. [CrossRef]
7. Zhou, D.; Zhang, Z.; Dong, H.; Liu, Y.; Hu, B.; Huang, S.; Zhang, X.; Lei, J.; Liu, N. In situ electronic modulation of g-C_3N_4/UiO_{66} composites via N species functionalized ligands for enhanced photocatalytic CO_2 reduction. *Sep. Purif. Technol.* **2025**, *379*, 134964. [CrossRef]
8. Zhang, Y.; Chen, J.; Buren, T.; Li, Z.; Zhang, X.; Ma, S.; Wei, J.; Bi, F.; Zhang, X. Electron beam irradiation defective UiO-66 supported noble metal catalysts for binary VOCs removal: Insight into the synergistic degradation mechanism of mutual promotion. *Sep. Purif. Technol.* **2025**, *380*, 135236. [CrossRef]
9. Bi, F.; Feng, X.; Huang, J.; Wei, J.; Wang, H.; Du, Q.; Liu, N.; Xu, J.; Liu, B.; Huang, Y.; et al. Unveiling the Influence Mechanism of Impurity Gases on Cl-Containing Byproducts Formation during VOC Catalytic Oxidation. *Environ. Sci. Technol.* **2025**, *59*, 15526–15537. [CrossRef]
10. Guo, L.; Li, Z.; Guo, M.; Lu, Z.; Bi, F.; Wang, Y.; Zhang, X. Study on the difference in catalytic performance and chlorine-resistance of Universitetet i Oslo-derived M@ZrO_2 (M = Pd, Pt) catalysts for o-Xylene degradation. *Mater. Today Chem.* **2025**, *49*, 103046. [CrossRef]
11. Yang, Y.; Ye, J.; Zhai, Y.; Yang, B.; Yin, M.; Xu, Y.; Wang, J.; Zhang, X. ZIF-67-derived monolithic bimetallic sulfides as efficient persulfate activators for the degradation of ofloxacin. *Surfaces Interfaces* **2024**, *51*, 104713. [CrossRef]
12. Yang, J.; Guo, S.; Dong, H.; Liu, Y.; Wang, J.; Quan, G.; Zhang, X.; Lei, J.; Liu, N. Enhanced visible-light-driven photocatalysis of ibuprofen by NH_2 modified MIL-53(Fe) graphene aerogel: Performance, mechanism, pathway and toxicity assessment. *Colloids Surfaces A Physicochem. Eng. Asp.* **2025**, *726*, 137769. [CrossRef]
13. Zhang, Z.; Dong, H.; Zhou, D.; Tang, K.; Ma, Y.; Han, T.; Lei, J.; Huang, S.; Zhang, X.; Tang, L.; et al. Electron beam- induced defect engineering construction in MIL-68(In) for enhanced CO_2 photoreduction: Unravelling organic framework defects. *J. Colloid Interface Sci.* **2025**, *702*, 138990. [CrossRef] [PubMed]
14. An, W.; Li, X.; Ma, J.; Ma, L. Advanced treatment of industrial wastewater by ozonation with iron-based monolithic catalyst packing: From mechanism to application. *Water Res.* **2023**, *235*, 119860. [CrossRef]
15. Shahzad, R.; Muneer, M.; Khalid, R.; Amin, H.M.A. ZnO-Bi_2O_3 Heterostructured Composite for the Photocatalytic Degradation of Orange 16 Reactive Dye: Synergistic Effect of UV Irradiation and Hydrogen Peroxide. *Catalysts* **2023**, *13*, 1328. [CrossRef]
16. Zhang, S.; Lin, Y.; Li, Q.; Jiang, X.; Huang, Z.; Wu, X.; Zhao, H.; Jing, G.; Shen, H. Remarkable performance of N-doped carbonization modified MIL-101 for low-concentration benzene adsorption. *Sep. Purif. Technol.* **2022**, *289*, 120784. [CrossRef]
17. Bai, X.; Zhang, M.; Shen, Y.; Liang, X.; Jiao, W.; He, R.; Zou, Y.; Chen, H.; Zou, X. Room-Temperature, Meter-Scale Synthesis of Heazlewoodite-Based Nanoarray Electrodes for Alkaline Water Electrolysis. *Adv. Funct. Mater.* **2024**, *34*, 2400979. [CrossRef]
18. Lin, J.; Liu, J.; Shao, L.; Shi, X.; Xu, J.; Guo, W.; Sun, Z.; Chen, C.; Hang, L. Regulating d–p Orbital Hybridized Electronic Structure via Doping Engineering for Advanced Sodium-Ion Batteries. *ACS Appl. Mater. Interfaces* **2025**, *17*, 38089–38099. [CrossRef]

19. Liu, W.; An, L.; Li, P.; Fu, Y.; Zhang, X.; Qu, D.; Liu, Y.; Hu, P.; Wang, X.; Jiang, N.; et al. Regulating electronic density and interfacial electric field of high-entropy metallenes to enhance oxygen reduction reaction activity. *Chem Catal.* **2025**, *5*, 101357. [CrossRef]
20. Liu, X.; Zhu, Y.; He, M.; Zhang, C.; Zuo, G.; Wang, Y.; Yang, S.; He, H. MOFs-derived Fe Ni bimetallic phosphide with tightly coupled heterogeneous interface for PMS activation. *Chem. Eng. J.* **2025**, *521*, 166974. [CrossRef]
21. Qiao, X.; Zhu, Q.; Hou, G.; Pang, Z.; Kang, H. Pinning effect of lattice co enhances lattice oxygen regeneration in NiFe-LDH for oxygen evolution reaction. *J. Colloid Interface Sci.* **2025**, *699*, 138219. [CrossRef] [PubMed]
22. Oglou, R.C.; Ceccato, M.; Frederiksen, M.L.; Shavorskiy, A.; Bentien, A.; Lauritsen, J.V. Depth-Profiling Cation Location and Oxidation States of Ni Foam Electrodes in Fe/Co-Enriched Electrolytes under Alkaline Water Oxidation Conditions. *ACS Catal.* **2025**, *15*, 17122–17132. [CrossRef]
23. He, S.; Zhang, R.; Han, X.; Zhou, Y.; Zheng, C.; Li, C.; Xue, X.; Chen, Y.; Wu, Z.; Gan, J.; et al. Unraveling 3d Transition Metal (Ni, Co, Mn, Fe, Cr, V) Ions Migration in Layered Oxide Cathodes: A Pathway to Superior Li-Ion and Na-Ion Battery Cathodes. *Adv. Mater.* **2025**, *37*, e2413760. [CrossRef] [PubMed]
24. Wang, Y.; Guo, X.; Zhao, Y.; Xu, Z.; Fan, S.; Long, H.; Fan, Q.; Duan, Z.; Zhang, J.; Jin, Z. The anodic chlorine ion repelling mechanisms of Fe/Co/Ni-based nanocatalysts for seawater electrolytic hydrogen production. *Nano Energy* **2025**, *135*, 110662. [CrossRef]
25. Bi, Q.; Zhang, Y.; Zhang, C.; Wang, K.; Zhao, S.; Xue, J. Precise control of cobalt active site size to switch ROS pathways: Millimeter-scale carbon beads derived from dual MOFs for targeted degradation of drug pollutants. *Appl. Catal. B Environ.* **2025**, *383*, 126046. [CrossRef]
26. Gu, D.; Zhong, W.; Li, C.; Xia, Y.; Zhu, Q. TiO_2-loaded porphyrin-like metal-organic framework as a heterojunction-peroxymonosulfate activated co-catalyst for bisphenol A removal. *Chem. Eng. J.* **2025**, *519*, 165169. [CrossRef]
27. Wang, C.; Lv, Z.; Deng, J.; Cao, T.; Kim, M.; Kang, H.; Wang, J.; Peng, R.; Zhu, X.; Mao, Y. ZIF-67-natural sponge derived macroarchitectures as efficient catalytic converters for 4-nitrophenol removal. *Chem. Eng. J.* **2024**, *498*, 155103. [CrossRef]
28. Wang, J.; Yao, J.; Yin, L.; Wang, B.; Liu, X.; Yuan, L.; Zhang, C.; Bao, T.; Liu, C.; Hu, X. Facet engineering of metal-organic frameworks for efficient tetracycline degradation by photocatalytic activation of peroxymonosulfate. *Chem. Eng. J.* **2024**, *497*, 154836. [CrossRef]
29. Zhang, X.; Pan, Y.; Wang, Y.; Wu, T.; Shao, B.; He, Q.; Zhou, L.; Li, T.; Liu, S.; Huang, X.; et al. MOF derived MnFeOX supported on carbon cloth as electrochemical anode for peroxymonosulfate electro-activation and persistent organic pollutants degradation. *Chem. Eng. J.* **2024**, *481*, 148646. [CrossRef]
30. Li, X.; Li, L.; Zhang, Z.; Ma, Y.; Smith, R.L.; Guo, H.; Zhao, R.; Liu, Y.; Yang, F.; Ding, Y. Insights into the mechanism of mechanically treated Fe/Mn-N doped seed meal hydrochar for efficient adsorption and degradation of tetracycline. *Biochar* **2025**, *7*, 1–17. [CrossRef]
31. O'Neill, S.J.; Ashizawa, M.; McLean, A.M.; Serrano, R.R.; Shimura, T.; Agetsuma, M.; Tsutsumi, M.; Nemoto, T.; Parmenter, C.D.J.; McCune, J.A.; et al. Supramolecular Conductive Hydrogels With Homogeneous Ionic and Electronic Transport. *Adv. Mater.* **2025**, *37*, e2415687. [CrossRef] [PubMed]
32. Sun, A.; Lu, J.; Liu, T.; Feng, C.; Liu, Y.; Pang, J.; Chen, L.; Wu, Z.; Han, S.; Li, Z. Characterization and mechanism of action of bimetallic-modified MIL-101(Fe) magnetic composites for enhanced removal of polystyrene from water. *Sep. Purif. Technol.* **2025**, *372*, 133397. [CrossRef]
33. Yang, L.; Wei, W.; Liu, Z.; Rae, R.; Santori, G.; Lau, C.H.; Qian, J.; Fan, X. Synergistic effects of salt and MIL-101(Cr) in composites: Unravelling the moisture pump-reservoir mechanism for efficient atmospheric water harvesting. *Chem. Eng. J.* **2025**, *524*, 169136. [CrossRef]
34. Zheng, F.; Lu, J.; Zheng, H.; Zhao, B.; Zhou, Z. Organic ligand-engineered MOFs-derived spinel $CoMn_2O_4$ with tailored nanostructures and chemical properties for synergistic low-temperature removal of NOx and VOCs. *J. Hazard. Mater.* **2025**, *496*, 139371. [CrossRef]
35. Saady, N.M.C.; Sivaraman, S.; Venkatachalam, P.; Zendehboudi, S.; Zhang, Y.; Palma, R.Y.; Shanmugam, S.R.; Espinoza, J.E.R. Effect of veterinary antibiotics on methane yield from livestock manure anaerobic digestion: An analytical review of the evidence. *Rev. Environ. Sci. Bio/Technol.* **2024**, *23*, 133–161. [CrossRef]
36. Shu, J.; Wu, Y.; Deng, Y.; Lei, T.; Huang, J.; Han, Y.; Zhang, X.; Zhao, Z.; Wei, Y.; Chen, M. Enhanced removal of Mn^{2+} and NH^{4+}-N in electrolytic manganese metal residue using washing and electrolytic oxidation. *Sep. Purif. Technol.* **2021**, *270*, 118798. [CrossRef]
37. Wan, Z.; Liu, X.; Li, H.; Chen, Y.; Hu, H.; Tong, X.; Duan, Y. Catalytic oxidation of peroxymonosulfate by Co/Fe loaded carbon nitride on oxidising SO_3^{2-} and inhibiting Hg0 release in solution. *Sep. Purif. Technol.* **2025**, *374*, 133682. [CrossRef]
38. Xin, J.; Wang, L.; Wang, X.; Miao, R.; Wang, J.; Sun, H.; Hao, J. Selective separation of Ni^{2+}/Co^{2+}/Mn^{2+} enabled by tunable intrapore sulfonic acid group content in covalent organic framework membranes via EDTA-chelation-assisted process. *J. Membr. Sci.* **2025**, *732*, 124252. [CrossRef]

39. Tan, C.; Cheng, X.; Xu, T.; Chen, K.; Xiang, H.; Su, L. Crystalline boron significantly accelerates Fe(III)/PMS reaction as an electron donor: Iron recycling, reactive species generation, and acute toxicity evaluation. *Chem. Eng. J.* **2022**, *452*, 139154. [CrossRef]
40. Rebstock, J.A.; Rao, A.; Samanta, A.; Asthagiri, A.; Baker, L.R. Specifically Adsorbed Carbonate Ions and Copper Surface Reconstruction: The Effect of Double Layer Charging Revealed by Time-Resolved Sum Frequency Generation Spectroscopy. *J. Am. Chem. Soc.* **2025**, *147*, 41404–41412. [CrossRef]
41. Yan, Y.; Spear, N.J.; Cummings, A.J.; Khusainova, K.; Macdonald, J.E.; Haglund, R.F. Harmonic-induced plasmonic resonant energy transfer between metal and semiconductor nanoparticles. *Sci. Adv.* **2025**, *11*, eadv1822. [CrossRef] [PubMed]
42. Li, X.; Chen, J.; Liu, Z.; He, C.; Pang, J.; Zhang, L.; Tang, F.; Yang, X. Recognizing the relevance of non-radical peroxymonosulfate activation by co-doped Fe metal-organic framework for the high-efficient degradation of acetaminophen: Role of singlet oxygen and the enhancement of redox cycle. *Chem. Eng. J.* **2024**, *499*, 156081. [CrossRef]
43. Gu, A.; Chen, K.; Zhou, X.; Gong, C.; Wang, P.; Jiao, Y.; Mao, P.; Chen, K.; Lu, J.; Yang, Y. Trimetallic MOFs-derived Fe-Co-Cu oxycarbide toward peroxymonosulfate activation for efficient trichlorophenol degradation via high-valent metal-oxo species. *Chem. Eng. J.* **2023**, *468*, 143444. [CrossRef]
44. Amin, H.M.A.; Attia, M.; Tetzlaff, D.; Apfel, U. Tailoring the Electrocatalytic Activity of Pentlandite $Fe_xNi_{9-X}S_8$ Nanoparticles via Variation of the Fe: Ni Ratio for Enhanced Water Oxidation. *ChemElectroChem* **2021**, *8*, 3863–3874. [CrossRef]
45. Farhat, R.; Dhainy, J.; Halaoui, L.I. OER Catalysis at Activated and Codeposited NiFe-Oxo/Hydroxide Thin Films Is Due to Postdeposition Surface-Fe and Is Not Sustainable without Fe in Solution. *ACS Catal.* **2019**, *10*, 20–35. [CrossRef]
46. Liu, X.; Hou, W.; Huang, Y.; Zhao, H.; Song, Z.; Huang, Y. Facile and green synthesis of carbon nanopinnacles for the removal of chlortetracycline: Performance, mechanism and biotoxicity. *Chem. Eng. J.* **2022**, *433*, 133822. [CrossRef]
47. Wang, L.; Wang, Y.; Wang, Z.; Du, P.; Xing, L.; Xu, W.; Ni, J.; Liu, S.; Wang, Y.; Yu, G.; et al. Proton transfer triggered in-situ construction of C=N active site to activate PMS for efficient autocatalytic degradation of low-carbon fatty amine. *Water Res.* **2023**, *240*, 120119. [CrossRef]
48. Zhi, K.; Liu, D.; Xu, J.; Li, Z.; Li, S.; Luo, L.; Gong, G.; Han, R.; Yin, A.; Guo, L. N-doped graphene loaded with Ru sites as PMS activators for SMX degradation via non-radical pathway: Efficiency, selectivity and mechanism. *Chem. Eng. J.* **2025**, *512*, 162230. [CrossRef]
49. Meng, Z.; He, Z.; Zhang, K.; Li, Y. Mechanism of NH3-SCR denitration catalyzed synergistically by Fe-Ce dual active sites in bastnäsite: A DFT study on the Fe-driven radical pathway and Ce oxygen vacancy regulation. *Mol. Catal.* **2025**, *586*, 115423. [CrossRef]
50. Yaseen, B.M.; Albadr, R.J.; Jain, V.; Kumar, A.; Ganesan, S.; Shankhyan, A.; Supriya, S.; Ray, S.; Taher, W.M.; Alwan, M.; et al. Modulating the Adsorption Properties of Benzene and Nitrobenzene Molecules on the Novel Ptn Cluster Modified C_3N Nanosheets for Sensing Applications: A Comparative DFT Investigation. *J. Inorg. Organomet. Polym. Mater.* **2025**, *35*, 6005–6017. [CrossRef]
51. Du, G.; Ma, S.; Yuan, K.; Chen, D.; Zhang, W.; Ding, H.; He, Z.; Fan, T.; Xu, E.; Li, Y. Oxygen vacancy-driven synergistic photocatalytic and peroxymonosulfate activation over iron-doped titanium dioxide for ciprofloxacin degradation. *J. Environ. Chem. Eng.* **2025**, *13*, 118516. [CrossRef]
52. Gu, Q.; Li, M.; Huo, Y.; Zhou, Y.; Ma, Y.; Wen, N.; He, M. Radical and non-radical pathways of organic arsenic removal in the heterogeneous peroxymonosulfate (PMS) activation system: A DFT study. *J. Clean. Prod.* **2025**, *525*, 146611. [CrossRef]
53. Wang, C.; Tian, J.; Cui, Y.; Li, N.; Cui, X.; Yan, B.; Chen, G. Synergy of CoN_3 and CuN_3O_2 sites in single atom-decorated biochar for peroxymonosulfate activation: Accelerating the production of $SO_4^{\bullet-}$ and •OH. *Chem. Eng. J.* **2024**, *496*, 154133. [CrossRef]
54. Li, T.; Li, H.; Wei, J.; Lu, Y.; Jing, Q.; Liang, M.; Zhou, H.; Zhang, G. Durable flame retardant containing a -C=C-P(=O)-O-C group with π–π conjugation for cotton fabrics. *Polym. Degrad. Stab.* **2025**, *233*, 111189. [CrossRef]
55. Wang, Q.; Jiang, Y.; Lin, X.; Li, H.; Wang, Z.; Wang, W. Insight into novel Fe_3C/Mo_2C@carbonized polyaniline activated PMS for parachlorophenol degradation: Key roles of Mo^{2+}, C=O bonds and N-doping. *Sep. Purif. Technol.* **2023**, *322*, 124359. [CrossRef]
56. Xiong, Y.; Chen, B.; Xu, T.; Zhou, Y.; Gao, P.; Bao, J. Modulation of C=O groups concentration in carbon-based materials to enhance peroxymonosulfate activation towards degradation of organic contaminant: Mechanism of the non-radical oxidation pathway. *Environ. Res.* **2025**, *275*, 121442. [CrossRef]
57. Wang, J.; Chu, Z.; Liu, H.; Han, Z.; Chen, T.; Zou, X.; Chen, D. Comparative study of chloroquine phosphate degradation by calcite/PMS and dolomite/PMS systems. *Sep. Purif. Technol.* **2025**, *380*, 135431. [CrossRef]
58. Liu, S.; Zhang, Z.; Huang, F.; Liu, Y.; Feng, L.; Jiang, J.; Zhang, L.; Qi, F.; Liu, C. Carbonized polyaniline activated peroxymonosulfate (PMS) for phenol degradation: Role of PMS adsorption and singlet oxygen generation. *Appl. Catal. B Environ.* **2021**, *286*, 119921. [CrossRef]
59. Karamad, M. Insights into C–N Bond Formation through the Coreduction of Nitrite and CO_2: Guiding Selectivity Toward C–N Bond. *ACS Catal.* **2025**, *15*, 8497–8510. [CrossRef]

60. Cui, J.; Gao, X.; He, B.; Yao, Y.; Zhao, Y.; Wang, T.; Yin, X. ZIFs material-derived bimetallic oxide heterojunctions activate perodisulfate to degrade chlortetracycline rapidly: The synergistic effects of oxygen vacancies and rapid electron transfer. *Chem. Eng. J.* **2024**, *483*, 149436. [CrossRef]
61. Liu, Z.; Jiang, B.; Sun, Z. Mechanism of self-supporting montmorillonite composite material for bio-enhanced degradation of chlorotetracycline: Electron transfer and microbial response. *Bioresour. Technol.* **2024**, *404*, 130928. [CrossRef]
62. Wang, C.; Li, X.; Lv, X.; Huang, X.; Zhao, Y.; Deng, T.; Zhang, J.; Wan, J.; Zhen, Y.; Wang, T. Insight into photocatalytic chlortetracycline degradation by WO_3/AgI S-scheme heterojunction: DFT calculation, degradation pathway and electron transfer mechanism. *J. Clean. Prod.* **2024**, *472*, 143521. [CrossRef]
63. Yin, B.; Guo, W.; Dong, H.; Meng, D.; Zhu, X.; Zhang, G.; Zhang, G.; Xin, Y.; Chen, Q. Construction of piezoelectric fenton-like system over $BaTiO_3$/α-FeOOH for highly efficient degradation of demethylchlortetracycline. *Sep. Purif. Technol.* **2024**, *359*, 130471. [CrossRef]

Disclaimer/Publisher's Note: The statements, opinions and data contained in all publications are solely those of the individual author(s) and contributor(s) and not of MDPI and/or the editor(s). MDPI and/or the editor(s) disclaim responsibility for any injury to people or property resulting from any ideas, methods, instructions or products referred to in the content.